ACS OMEGA

Article

Cite This: ACS Omega 2018, 3, 10877−10885

http://pubs.acs.org/journal/acsodf

NIR-Light-Active ZnO-Based Nanohybrids for Bacterial Biofilm Treatment

Damayanti Bagchi,[†] V. S. Sharan Rathnam,[‡] Peter Lemmens,[§] Indranil Banerjee,[‡] and Samir Kumar Pal*[,†]

[†]Department of Chemical, Biological and Macromolecular Sciences, S. N. Bose National Centre for Basic Sciences, Block JD, Sector III, Salt Lake, Kolkata 700106, India

[‡]Department of Biotechnology and Medical Engineering, National Institute of Technology, Rourkela 769008, Odisha, India

[§]Institute for Condensed Matter Physics and Laboratory for Emerging Nanometrology, TU Braunschweig, Mendelssohnstrasse 3, 38106 Braunschweig, Germany

Supporting Information

ABSTRACT: Nanomaterials with antimicrobial properties triggered by external stimuli appear to be a promising and innovative substitute for the destruction of antibiotic-resistant superbugs as they can induce multiple disruptions in the cellular mechanism. This study demonstrates the use of squaraine (SQ) dye as the photosensitive material, activated in the near-infrared tissue-transparent therapeutic window. The dye has been covalently attached to the ZnO nanoparticle surface, forming ZnO-SQ nanohybrids. The formation of the nanohybrids is confirmed using Fourier transform infrared and other optical spectroscopic methods. The photoinduced interfacial electron transfer process (as confirmed using the time-resolved fluorescence technique) from the excited state of SQ to the conduction band of ZnO is responsible for the greater reactive oxygen species (ROS) generation ability of the nanohybrid. The production of photoactivated ROS (especially singlet oxygen species) by ZnO-SQ provides remarkable antimicrobial action against clinically significant *Staphylococcus aureus*. Detailed investigations suggest synergistic involvement of cell membrane disruption and nanoparticle internalization followed by photoinduced intracellular ROS generation, which result in an unprecedented 95% bacterial killing activity by the nanohybrid. Moreover, the efficacy of the nanohybrid for disruption of bacterial biofilms has been examined. The electron microscopic images suggest significant bacterial cell death following structural alteration and reduced adherence property of the biofilms. Nanodimension-driven greater internalization of ZnO-SQ followed by an improved dissolution of ZnO in an acidic environment of the biofilm as well as red-light-driven interfacial charge separation and ROS generation improves the efficacy of the material for biofilm destruction. An artificial medical implant mimicking titanium sheets coated with ZnO-SQ depicts light-triggered disruption in the adherence property of matured biofilms. The cytotoxicity and hemolysis assays show inherent biocompatibility of the photoactive nanohybrid. This study is notably promising for the treatment of life-threatening drug-resistant infections and eradication of biofilms formed within artificial implants.

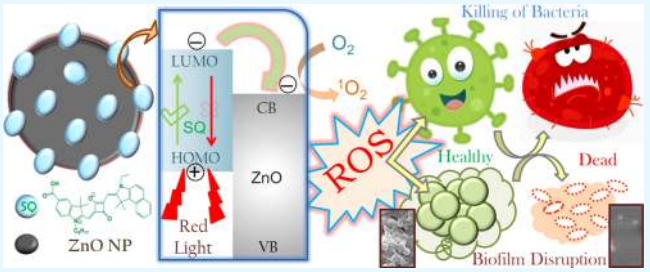

1. INTRODUCTION

The utilization of nanomaterials for various biomedical aspects such as biosensors, drug delivery, theranostics, and diagnosis is currently undergoing a dramatic expansion.[1] Nanomaterials, due to their dimension-driven extraordinary physical and chemical properties, have appeared as a potential platform either being a delivery vehicle to transport drugs at the diseased site or as an active therapeutic agent.[2] However, the potential toxicity of nanomaterials upon long-term exposure is questionable and such treatments would be applied selectively for inhibiting the affected tissues while leaving the surrounding host cells healthy and intact.[3] This requires the nanoparticles (NPs) to be activated in the specific target organism.[4] Target specificity often depends on specific environmental signals such as temperature, pH, redox properties, enzymatic metabolism, etc., which could be regulated through the application of external stimuli such as chemical stimuli (pH) or physical stimuli (light).[5,6] Hence, development of stimuli-responsive nanomaterials is high on demand because of their multipurpose and highly efficacious implementations.[7−9]

Light-mediated treatment, namely, photodynamic therapy (PDT),[10] involves photosensitizers, which could be activated by photon energy followed by production of light-activated redox species and/or reactive oxygen species (ROS) for therapeutic use. The spatial and temporal localization using light sources provides prevention to potential side effects of the

Received: May 19, 2018
Accepted: July 10, 2018
Published: September 10, 2018

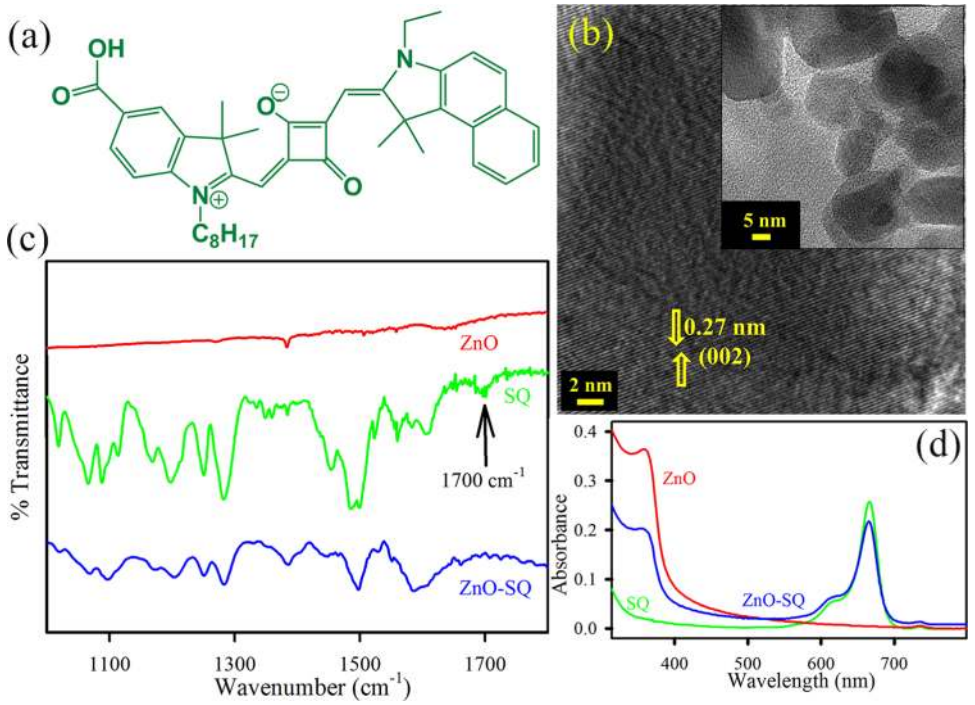

Figure 1. (a) Structure of SQ. (b) HRTEM image of ZnO NPs. Lattice fringes in the corresponding HRTEM image indicate high crystallinity. The inset shows the transmission electron microscopy (TEM) images of ZnO NPs. (c) FTIR spectra of ZnO NPs (red), SQ (green), and ZnO-SQ (blue). (d) UV−vis absorption of ZnO NPs (red), SQ (green), and ZnO-SQ (blue) in DMSO.

therapies. Moreover, the investigation of the therapeutic efficacy of photoactive drugs using near-infrared light can provide new ways for using the biological window of optical transparency.[11] This often suggests implication of a NIR-absorbing dye molecule or nanomaterials as a photosensitizer in PDT, which in turn improves the penetration potency of the light used.[12,13] There are plenty of reports on multifunctional NIR agents for cancer targeting and imaging applications showing great potential for clinical use.[14]

The emergence of pathogenic bacteria with acquired multidrug resistance indicates the dawn of a postantibiotic era, an alarming crisis worldwide.[15,16] A recent report by the Centers for Disease Control and Prevention indicates that each year at least two million people suffer from bacterial infections that are resistant to antibiotics in the United States alone.[17] Different nanomaterials, such as silver nanoparticles (Ag NPs), depict unprecedented antimicrobial activities and are often consider as nanoantibiotics (nAbts), a term that has been coined for the nanomaterials that show direct antimicrobial activity or improve the effectiveness and safety of antibiotic administration.[18] nAbts are advantageous because of their sustained release and uniform distribution in the target tissue following enhanced cellular internalization, which minimize the possible side effects and patient compliance.[19] However, to minimize the possible side effects and complications introduced by nAbts, stimuli responsiveness is necessary.[20] In this regard, antimicrobial PDT (APDT) using nanomaterials shows huge potential.

Moreover, healthcare-associated infections comprising medical device-related catheter-associated urinary tract infections, lower respiratory tract infections, and surgical-site infections are often related to Gram-positive bacteria, such as *Staphylococcus aureus* and *Staphylococcus epidermidis* and their virulent biofilms.[21] Biofilms are dynamic communities of immobile bacteria encapsulated within a protective matrix of polysaccharides, proteins, nucleic acids, and lipids, developing a compact structure commonly attached to a surface or to each other.[22] The challenges in eradication of biofilms are presumably due to the existence of the extracellular polymeric substances, which prevent the penetration of small-molecule therapeutics into biofilms.[23,24] This often suggests the desperate need for innovative nanotherapeutics.[25] The eradication of bacterial biofilms can be achieved through nanomaterial coating on implant surfaces.[26] The systematic interactions of the biofilms with nanomaterials through efficient uptake and accumulation of antimicrobial agents into the biofilm network provide an enhanced therapeutic efficacy.[23]

The intrinsic acidic microenvironments of biofilms, chronic infections, or wounds (pH values 4−7) could be exploited to fabricate pH-sensitive nanotherapeutics.[27] The superior dissolution of zinc oxide nanoparticles (ZnO NPs) at lower pH inducted its use as nanocarriers for drug delivery application.[28] ZnO NPs also depict greater biocompatibility than that of other metal oxide NPs with size-dependent antimicrobial property.[29] Despite the promising prospect of ZnO NPs as drug delivery vehicles due to their low cost and lesser cytotoxicity, the wide-band-gap (~3.3 eV) semiconducting nature suggests its activation only by UV light ($\lambda \sim 375$ nm), which eventually restricts its clinical applications.[30] Inorganic metal oxide NPs conjugated with organic photosensitizers form a new class of nanohybrids showing superior activity than that of the individual counterparts.[31] The reports indicating the use of ZnO and visible-light-active photosensitizers (protoporphyrin, blue-light-active and rose bengal, green-light-active) and indicating enhanced ROS generation have previously been published by our group.[30] However, to utilize the biologically transparent NIR range absorption for

DOI: 10.1021/acsomega.8b00716
ACS Omega 2018, 3, 10877−10885

efficient PDT, we employed here a red-light-active dye squaraine (SQ2) as the active photosensitizer.

The present study depicts the use of red-light-absorbing dye squaraine (SQ) as the photosensitizer for APDT. The dye molecule has been conjugated to the ZnO NP surface, which has been confirmed using optical and vibrational (Fourier transform infrared (FTIR)) spectroscopy tools. The nanohybrids employ both the stimuli-responsive nature and acidic pH sensitivity due to ZnO and NIR light sensitivity due to the SQ dye. The molecular-level interaction between two moieties initiates the photoinduced excited-state electron transfer process from dye to ZnO, which indeed improves the ROS generation capability. The improvement of in vitro activity facilitates the dose-dependent killing of Gram-positive bacteria (*S. aureus*) through cell membrane rupture and cellular internalization. We have also employed the ZnO-SQ nanohybrid for eradication of biofilms. The crystal violet (CV) assay was performed to analyze the antibiofilm activity. We have further used scanning electron microscopy (SEM) to observe the structural alteration of the biofilm upon photodynamic treatment. The material is eventually coated over titanium sheets (used as mimic implants[32]), and their antibiofilm activity has been evaluated. The nanohybrids also depict low toxicity to human cells and maintain high hemocompatibility.

2. RESULTS AND DISCUSSION

The structure of the asymmetric squaraine (SQ) dye is depicted in Figure 1a. Figure 1b depicts the high-resolution transmission electron microscopy (HRTEM) image of ZnO NPs. The lattice fringes of ZnO NPs show an interplanar distance of 0.27 nm, which corresponds to the (002) crystal planes. The overall size distribution of ZnO NPs is shown in the inset of Figure 1b. The average particle dimension is found to be ∼24 nm. To confirm the conjugation of SQ to ZnO NP surfaces, the Fourier transform infrared (FTIR) technique has been used. The free SQ possesses stretching frequencies at 1486 cm^{-1}, which is attributed to the C═C stretching in the four-membered ring,[33] and at 1700 cm^{-1}, the typical peak for the C═O stretching of an aromatic carboxylic group (Figure 1c). This latter signal clearly disappears in the ZnO-SQ conjugated system, keeping other signals unaltered, suggesting that SQ is attached to the semiconductor surface through the peripheral COOH binding of SQ to ZnO. The conjugation between SQ and ZnO NPs can also be understood by UV−vis spectroscopy (Figure 1d). The absorption spectra of SQ in dimethyl sulfoxide (DMSO) show a noticeable peak at 665 nm, which corresponds to the $\pi-\pi^*$ charge-transfer process with a minor peak at 615 nm of dye aggregation.[34] The characteristic peaks of both SQ and ZnO are observed in the ZnO-SQ nanohybrids, which indicate the successful complexation between the two moieties. The steady-state photoluminescence (PL) spectra of SQ and ZnO-SQ in DMSO are shown in Figure 2a, and the corresponding excitation spectra are presented in the inset of Figure 2a. SQ exhibits emission maxima at 673 nm upon excitation at 633 nm. The emission intensity is significantly reduced after attachment of SQ to the ZnO NPs. These results imply the presence of nonradiative decay processes from SQ to ZnO NPs. The excitation spectra depict two peaks for SQ, which are similar to the corresponding absorption spectra. The ZnO-SQ nanohybrid shows 5 nm bathochromic shift in the excitation spectra, indicating molecular-level interaction during the attachment process. To further study the electronic interactions, time-resolved fluorescence transient studies have been carried out.[35] The lower-density sp orbital of Zn^{2+} in ZnO interacts with lowest unoccupied molecular orbital of dye (SQ), suggesting an ultrafast sub-picosecond time scale due to the electron injection process.[36] The fluorescence decay transients for free SQ and ZnO-SQ have been collected upon excitation at 633 nm and detected at 670 nm (Figure 2b) using DMSO as the solvent. The decay constants for the excited-state decay profiles of SQ in DMSO show single exponential decay, with a lifetime of 580 ps. A very fast time component of 30 ps generates after attachment of SQ on ZnO surfaces, suggesting a photoinduced electron transfer process from the excited state of SQ (dye) to the conduction band of ZnO NPs (semiconductor surface). The details of the fitting parameter of the fluorescence decays are provided in Table 1. As the ZnO NPs used in the present study have not shown any intrinsic defect state emission property, there is no chance of energy transfer process associated with the faster time scale present in the nanohybrids. Scheme S1 depicts the band energy gap diagram and charge distribution at the ZnO-SQ interface.

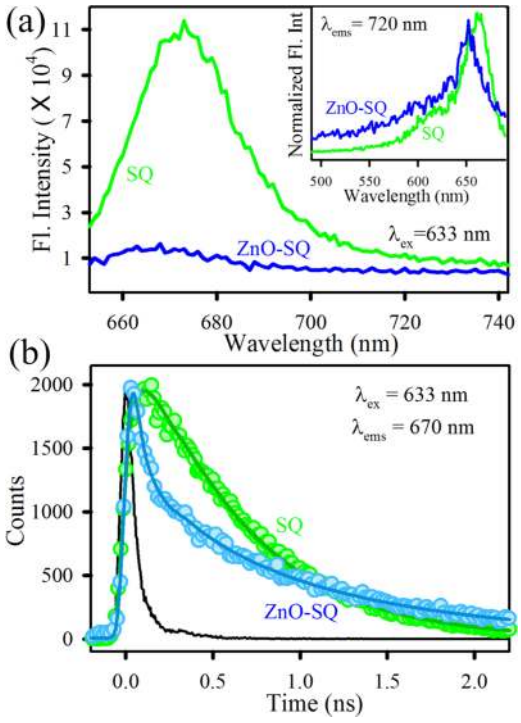

Figure 2. (a) Room-temperature PL spectra (excitation at 633 nm) of SQ (green) and ZnO-SQ (blue). The inset shows the normalized excitation spectra of SQ (green) and ZnO-SQ (blue) at a detection wavelength 720 nm. (b) Fluorescence decay profiles of SQ (green) and ZnO-SQ (blue) at 670 nm (excitation at 633 nm).

The efficient electron transfer process present in ZnO-SQ motivates us to investigate the photoinduced ROS generation capability of the nanohybrid. The ROS production ability of the sample has been evaluated using the DCFH assay in which the oxidation of DCFH (nonfluorescent) to dichlorofluorescein (DCF, fluorescent) through interaction with ROS is monitored.[37] The fluorescence emission intensity of DCF is recorded with respect to (wrt) time (Figure 3a). The highest enhancement of the fluorescence intensity of DCF is obtained for ZnO-SQ nanohybrids under red light irradiation. ROS production increases three times compared to that with free dye SQ. The control experiments with DCFH and ZnO under

DOI: 10.1021/acsomega.8b00716
ACS Omega 2018, 3, 10877−10885

Table 1. Picosecond-Resolved Fluorescence Transient Lifetime[a]

systems (ex-633−ems-670)	τ_1 (ps)	τ_2 (ps)	τ_3 (ps)	τ_{avg} (ns)
SQ	580 (100%)			0.58
ZnO-SQ	30 (78.3%)	364.7 (6.7%)	1111.8 (14.9%)	0.21

[a]Numbers in parentheses indicate relative contributions.

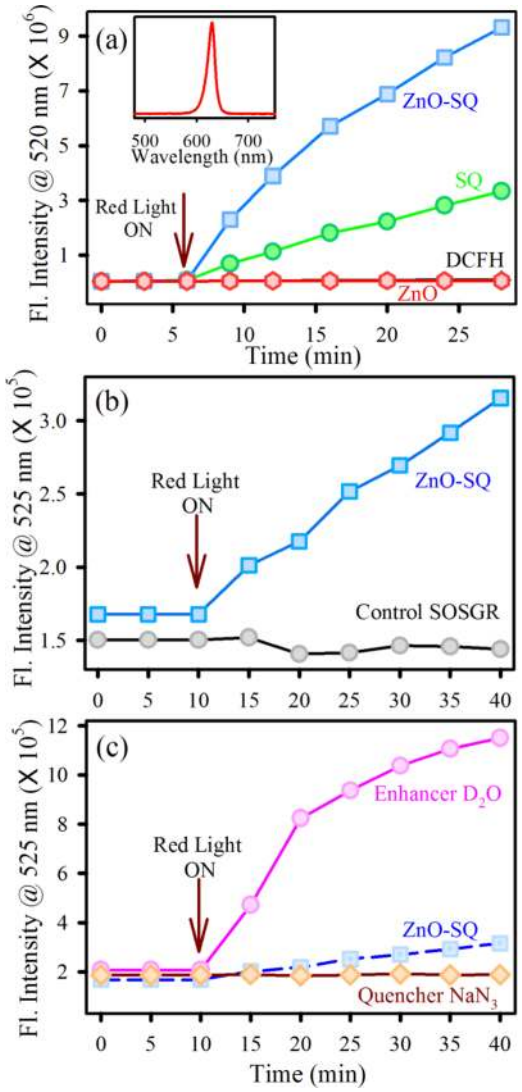

Figure 3. (a) DCFH oxidation with respect to time in the presence of SQ (green), ZnO-SQ (blue), ZnO (red), and only control DCFH (black) under dark followed by red light irradiation. The excitation was at 640 nm. (b) Fluorescence response of SOSGR in the presence of ZnO-SQ (blue) and control SOSGR (black) under dark followed by red light irradiation. (c) Fluorescence response of SOSGR in the presence of enhancer D_2O (pink) and quencher NaN_3 (dark red) with the sample ZnO-SQ under dark followed by red light irradiation. The dotted blue line shows the fluorescence response of SOSGR in the presence of ZnO-SQ.

red light irradiation show negligible increase in fluorescence intensity. This confirms the involvement of photoinduced interfacial charge transfer dynamics in ZnO-SQ for enhancement of ROS production. However, the DCFH assay is incompetent for the determination of specific nature of ROS. To confirm whether the generated ROS is singlet oxygen or not, we have performed the singlet oxygen sensor green reagent (SOSGR) assay.[38] This also involves monitoring of the emission intensity at 525 nm with progressing time. Figure 3b depicts a significant increase in the fluorescence intensity of SOSGR when exposed to ZnO-SQ under red light illumination. Furthermore, a quencher (NaN_3) and an enhancer (D_2O) of singlet oxygen species are added with SOSGR and ZnO-SQ under red light illumination. In the case of D_2O, the fluorescence intensity increases many fold, whereas for NaN_3, it reduces significantly (Figure 3c). These results indeed confirm the generation of red-light-induced singlet oxygen by ZnO-SQ and signify its importance as a potential photodynamic agent for therapeutic action.

The ZnO-SQ nanohybrid was evaluated for its antimicrobial activity as a potential photodynamic agent for the inhibition of growth of *S. aureus*. The effect various concentrations (0−350 nM) of the sample on *S. aureus* growth has been examined using the colony-forming unit (CFU) assay under dark conditions (Figure 4a). The inhibition in bacterial growth was significant at a concentration of ∼200 nM, suggesting the use of lower concentration for determining the photodynamic

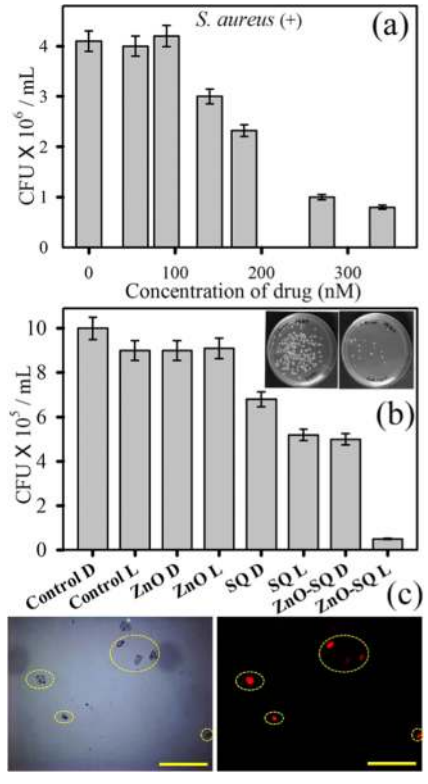

Figure 4. (a) Dose-dependent antibacterial effect of ZnO-SQ at concentrations ranging from 0 to 400 nM on *S. aureus* under dark conditions. (b) Bacterial viability after treatment with 140 nM ZnO-SQ in the presence and absence of red light irradiation. The inset shows images of *S. aureus* plates treated with ZnO-SQ, before (left) and after (right) red light irradiation. (c) Propidium iodide staining assays for cell membrane disruption of *S. aureus*. Microscopic images of *S. aureus* treated with ZnO-SQ under red light illumination: left panel, bright field and right panel, fluorescence. Scale bar is 100 μm.

DOI: 10.1021/acsomega.8b00716
ACS Omega 2018, 3, 10877−10885

action. We have employed 140 nM sample and incubated the bacterial culture for 3 h in the dark for cellular uptake of the drug followed by 30 min red light illumination. The pictures of *S. aureus* cultures (inset in Figure 4b) treated with the sample in the absence and presence of red light depict the visible change in bacterial growth after photodynamic treatment, with significantly less number of colonies. In control and ZnO-treated samples, no antibacterial activity under dark and light-irradiated conditions is observed. For SQ-treated samples, the bacterial growth is decreased up to 45% under light irradiation. The highest inhibition of bacterial growth is obtained for ZnO-SQ-treated samples with a 95% decrease in CFU after illumination (Figure 4b). To elucidate the mechanism behind the enormous photodynamic killing efficiency of ZnO-SQ, we first evaluate its photoinduced bacterial membrane distortion capacity. The bacterial cultures without sample treatment (under dark and with red light irradiation) and treated with ZnO-SQ (under dark and with red light irradiation) were stained with propidium iodide (PI) to check bacterial membrane integrity (Figure S1). PI penetrates only into cells with damaged membranes, which will enhance the fluorescence.[39] As shown in Figure 4c, red fluorescence was observed only from bacterial cells treated with ZnO-SQ followed by red light illumination, indicating membrane disruption due to photodynamic action of ZnO-SQ. Furthermore, we have evaluated the capability of ZnO-SQ to modulate the intracellular ROS generation, which promotes several cell death mechanisms. As shown in Figure 5a, we noted that ZnO-SQ-treated *S. aureus* induced about 2-fold increase in the intracellular ROS production under red light illumination conditions compared to that from the control group. Further extending our investigation, we have examined the bacterial morphology and NP internalization using transmission electron microscopy (TEM). As shown in Figure 5b, *S. aureus* exhibits typical membrane structures. The morphology and membrane integrity of the bacteria dramatically altered after photodynamic treatment with ZnO-SQ (Figure 5c). The NPs randomly adsorbed on bacteria, inducing noticeable changes in membrane morphologies. Significantly, the multilayered peptidoglycan coating of Gram-positive bacteria enhances the nanoparticle−biofilm interactions, leading to NP penetration. ZnO NPs are already shown to disturb lipids and proteins of the cell membrane, which results in bacterial cell death (Scheme S2).[40] The HRTEM image (shown in Figure 5d) at the cell membrane depicts internalization of highly crystalline ∼10 nm ZnO NPs into the bacterial cell. The overall distribution of the NPs consisting of ∼10 nm grain boundary in the cytoplasmic area clearly confirms cellular trafficking of the bigger NPs and embodiment of smaller NPs within the bacteria, which are responsible for drug delivery and photoinduced intracellular ROS generation following cell death. The diverse cell death mechanism owing to photodynamic therapy by ZnO-SQ is pictorially depicted in Figure 5e.

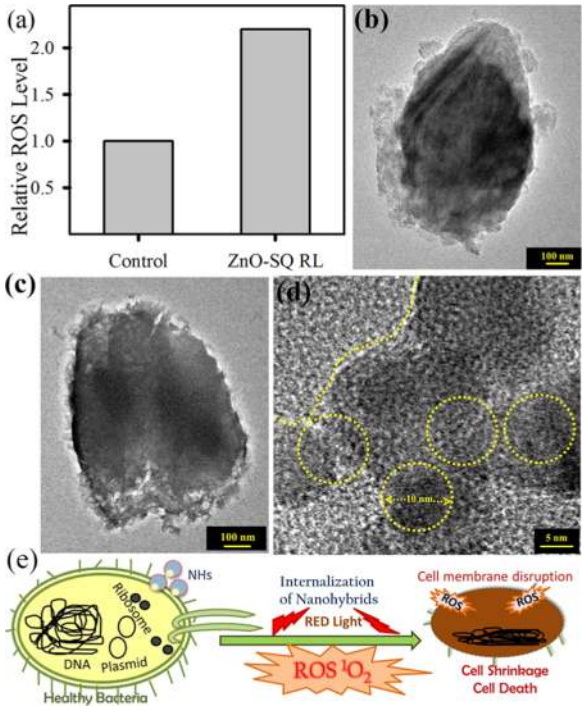

Figure 5. (a) Intracellular ROS of *S. aureus* after incubation with ZnO-SQ for 2 h followed by red light illumination of 30 min. (b) TEM image of *S. aureus*. (c) TEM image of *S. aureus* after ZnO-SQ incubation for 2 h followed by red light illumination for 30 min. (d) HRTEM image of the membrane of drug-treated *S. aureus*. Nanoparticle internalization is clearly visible. (e) Schematic representation of bacterial cell disruption by internalization and ROS generation of the nanohybrids.

The diverse cell death mechanism leading to an exceptional stimuli-responsive antimicrobial efficacy drives us to investigate the ability of ZnO-SQ to disrupt biofilm formation in a red-light-activated process. The adhered biomass of 48 h grown biofilms shows a decrease in biomass (∼20%) for the ZnO-SQ-treated samples. The bacterial biomass could be further reduced to ∼55% when ZnO-SQ-treated bacteria were exposed to red light for 30 min (Figure 6a). The upper panel of Figure 6a shows photographs of crystal violet stain in the Petri plates demonstrating visible reduction of biofilm adherence upon photodynamic treatment. The structural and morphological changes of the biofilms were observed by taking optical microscopy and scanning electron microscopy images. Figure 6b,c depicts the structure of the *S. aureus* biofilm without any treatment and with the ZnO-SQ red-light treatment, respectively. The inherent colonization property of bacterial biofilms is significantly perturbed upon the treatment. Moreover, Figure 6d shows typical characteristics of *S. aureus* biofilms comprising extracellular polymeric matrix, and Figure 6e shows biofilms treated with ZnO-SQ followed by red light irradiation, which contain significantly fewer bacteria without the typical arrangement of a biofilm. Upon treatment, both the adherence property and the characteristic morphology of the biofilm were completely destroyed. The antibiofilm activity of ZnO-SQ suggests that acidic-pH-responsive delivery vehicle ZnO (Figure S2) acts as a permeation enhancer, followed by a synergistic mechanism of internalization of NPs within biofilms and generation of photoactive ROS disrupts the biofilm structures completely. These findings suggest that ZnO-SQ should possess practical applicability for biofilm disruption on medical implants. To unravel the potential for clinical utilization, we have coated titanium sheets, the model for medical implants, with ZnO-SQ samples followed by 48 h incubation with the *S. aureus* culture (OD_{600} = 1). This generates bacterial biofilms over the coated titanium sheets, as indicated in Figure 7a, upper panel. The remarkable crystal violet staining over the coated titanium sheet demonstrates the presence of proliferating biofilms. However, as the sheet was

DOI: 10.1021/acsomega.8b00716
ACS Omega 2018, 3, 10877−10885

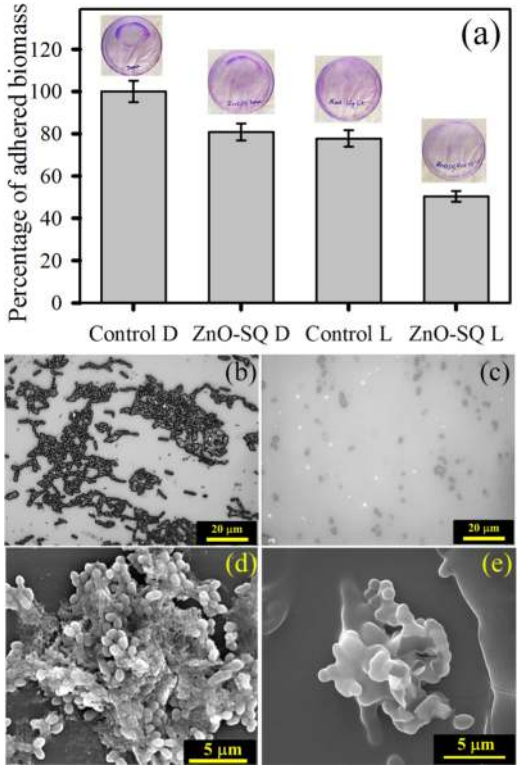

Figure 6. (a) Antibiofilm effects of ZnO-SQ on the *S. aureus* biofilm in the presence and absence of red light illumination monitored by the adhesion efficiency of biomass through the crystal violet staining assay. The upper panel shows images of crystal violet-stained plates. Microscopic images of (b) *S. aureus* biofilms and (c) biofilms after red light illumination on ZnO-SQ-treated samples. Scale bar is 20 μm. Field emission gun SEM images of (d) *S. aureus* biofilms and (e) biofilms after red light illumination on ZnO-SQ-treated samples. Scale bar is 5 μm.

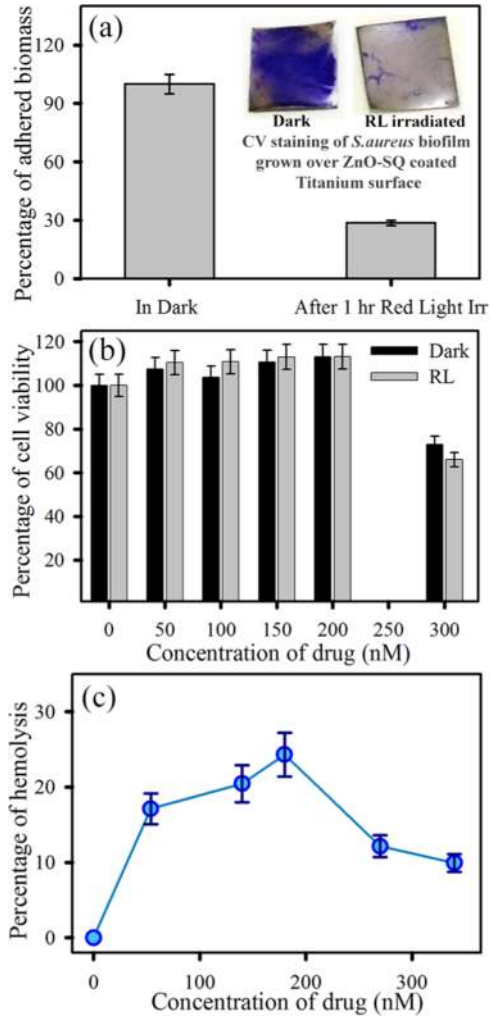

Figure 7. (a) Antibiofilm activity of the ZnO-SQ-sensitized model titanium sheet in the absence and presence of red light illumination. The upper panel depicts the visual change in crystal violet staining after treatment with red light. (b) Cytotoxicity assay in human bone cell MG-63 with different concentrations of ZnO-SQ in the absence and presence of red light illumination. (c) Hemolysis assay of ZnO-SQ at different concentrations under dark conditions.

illuminated under red light for 1 h, there is a significant reduction in crystal violet staining, suggesting disruption of biofilms due to photoinduced ROS generation by ZnO-SQ. This signifies the stimuli-responsive targeted photodynamic killing and disruption efficacy of bacterial biofilms by ZnO-SQ, suggesting future clinical prospect.

Nevertheless, the toxicity of nanomaterials toward mammalian cells is one of the critical points for in vivo application. For this, we first evaluated the toxicity of the nanohybrids against human osteoblast cell line MG-63. We have specifically chosen the bone fibroblast cells to evaluate the cytotoxicity as microbial biofilm pathogens are the causative agents of chronic osteomyelitis. As depicted in Figure 7b, MG-63 cells treated with various concentrations of nanohybrids had negligible cytotoxicity as measured using the 3-(4,5-dimethylthiazol-2-yl)-2,5-diphenyltetrazolium bromide (MTT) assay under both dark and red light irradiation conditions. The cell viability upon treatment with ZnO-SQ up to 200 nM concentration under both dark and red light illumination conditions is comparable (>95%) to that of the control cells (Figure 7b). The significant toxicity arises at 300 nM concentration (30 and 40% cell death in dark and light, respectively), which is double the concentration used for the antimicrobial assays. This result confirms appreciable biocompatibility of ZnO-SQ nanohybrids. Moreover, the hemolytic activity of these NPs against human red blood cells (RBCs) was measured. As shown in Figure 7c, at variable concentrations with highest dosing of twice the dose used for antimicrobial therapy, the NPs show no observable hemolytic activity, demonstrating the intrinsic biocompatibility of ZnO-SQ with human blood cells. The NPs are also biocompatible when exposed under red light (data not shown), suggesting the stimuli-responsive system as safe toward real-life implementation. These overall effects suggest ZnO-SQ as a stimuli-responsive biocompatible antimicrobial and antibiofilm agent, which demonstrates achievable clinical applications with respect to previously reported systems.

3. CONCLUSIONS

An antimicrobial photodynamic therapy (APDT) depends on target specificity of the drug and the penetration capability of the light used. In the present study, we have demonstrated the use of squaraine (SQ) as the red-light-activated photosensitizer, which can enhance the light penetration ability through tissue. SQ was successfully conjugated with ZnO NPs (~24 nm, confirmed by TEM) to impart pH sensitivity followed by nanodimension-driven drug internalization. The

DOI: 10.1021/acsomega.8b00716
ACS Omega 2018, 3, 10877−10885

attachment was confirmed using FTIR, UV−vis, steady-state fluorescence spectroscopy tools. The photoinduced excited-state electron transfer process from the dye to semiconductor was validated by time-resolved fluorescence transients, and this process leads to a greater extent of ROS generation. The ROS generated by ZnO-SQ is essentially singlet oxygen in nature as confirmed using the SOSGR assay. The photodynamic antibacterial effect on *S. aureus* was confirmed using the CFU assay, which suggests reduction of 95% CFU after light-activated drug treatment. The immense bacterial killing activity generated due to cell membrane disruption was confirmed by the PI staining fluorescence microscopy-based assay, and cellular internalization of NPs was demonstrated using TEM and intracellular ROS generation. The tremendous stimuli-responsive effectiveness of ZnO-SQ for killing bacteria drew our attention to check its efficacy to eradicate bacterial biofilms. The quantitative crystal violet assay depicted photoactivated antibiofilm effect of the nanohybrids. The loss of adherence property in biofilms as well as the structural disruption was confirmed using microscopic images. The ZnO-SQ nanohybrid was coated over titanium metal sheets, used as artificial implant mimic, and was demonstrated to eradicate mature biofilms by application of external red illumination. The cytotoxicity assay using human bone cell line MG-63 and the hemolysis assay on human RBCs show intrinsic biocompatibility of ZnO-SQ, suggesting its overall clinical applicability. Hence, this enquiry could be translated to develop penetrable light-activated nanoantibiotic agents to treat antibiotic-resistant clinically isolated pathogens.

4. EXPERIMENTAL DETAILS

Analytical-grade reagents were utilized for the synthesis without further purification. ZnO NPs were obtained from Sigma-Aldrich. X-ray fluorescence analysis suggests >97 wt % zinc, and the particle size is <50 nm, as confirmed by Brunauer−Emmett−Teller.[41] The squaraine dye (sensidizer SQ2) was purchased from Solaronix. The suitable solvent used for preparing the dye solution was DMSO (Merck). Millipore water was used to prepare the aqueous solution. Titanium foils (Sigma-Aldrich) of 1 cm × 1 cm dimensions were used as mimic implants.

4.1. Preparation of SQ-Sensitized ZnO Nanohybrids. The nanohybrids were prepared using overnight incubation of 0.5 mM SQ with ZnO NPs under dark conditions. After the sensitization process, the solution was centrifuged and washed with DMSO four times to separate any unattached dye. The nanohybrid was then dried in an oven and stored in the dark until further use.

4.2. Characterization Techniques. Diluted solutions of ZnO NPs were spread over carbon-coated copper grids for TEM analysis. The particle sizes were determined from micrographs using an FEI (Technai S-Twin, operating at 200 kV) instrument at a magnification of 100 000×. The FTIR spectra were recorded on a JASCO FTIR-6300 spectrometer. A Shimadzu spectrophotometer (UV-2600) was used for measuring absorption, and a HORIBA Fluorolog was employed to measure steady-state emission. Time-resolved photoluminescence measurements were carried out through a time-correlated single-photon counting setup from Edinburgh Instruments. The measured instrument response function was 60 ps, and excitation at 633 nm was used while emission was detected at 670 nm. The fitting of the fluorescence transients was done using a nonlinear least-squares procedure, as reported in our previous publications.[42−44] For all light-activated experiments, a red light-emitting diode (LED) source (λ_{max} = 640 nm and power = 3 mW/cm^2) was used.

4.3. In Vitro Measurement of ROS. DCFH was prepared from dichlorofluorescin diacetate (DCFH-DA; Calbiochem) using the reported de-esterification reaction procedure.[31] SQ (1 μM), ZnO (150 μM), and ZnO-SQ (individual concentrations of SQ and ZnO in the nanohybrid are 1 and 150 μM, respectively) were used for the assay. To infer the singlet oxygen generation, the singlet oxygen sensor green reagent (SOSGR)[38] from Molecular Probes was used. Furthermore, singlet oxygen quencher NaN_3 (Sigma) and enhancer D_2O (Cambridge Isotope Laboratories, Inc.) were employed for confirming the formation of singlet oxygen species.[45]

4.4. Bacterial Strain and Culture Conditions. The bacteriological assays were performed using the strain *S. aureus* (ATCC 25923), and details are provided in Supporting Information (SI). The cells were incubated with 140 nM nanohybrids (concentration is calculated wrt SQ loading, details are provided in SI) followed by red light illumination (λ_{max} = 640 nm) for 30 min. The photodynamic action was measured by using Luria−Bertani (LB) agar-based colony formation assay.

4.5. Propidium Iodide Staining Assay. *S. aureus* (1×10^8) cells were treated with 140 nM nanohybrid in the dark at 37 °C and 300 rpm for 3 h. Then, bacterial solutions were divided into two parts and one part was exposed to red light. After the treatment, samples were incubated with 2 μM PI for 15 min in the dark. The samples (10 μL) were observed under a fluorescence microscope (Leica digital inverted microscopes DMI8).

4.6. Intracellular ROS Determination. To confirm the unaltered efficacy of the nanohybrids in the presence of common biomolecules and metal ions, i.e., more like cellular conditions, we have assessed the intracellular ROS generation. In the assay, 10 μM DCFDA was added to the treated bacterial culture and incubated for 30 min in the dark. The samples were then centrifuged and washed with water. The emission intensity at 520 nm was analyzed upon 488 nm excitation.[46]

4.7. Internalization of Nanohybrids into Bacterial Cells: TEM Observations.[47] The nanohybrid-treated bacterial solution was applied to a carbon-coated Cu grid. After settlement of the solution in the grid, cells were stained with 2 μL of 1% uranyl acetate for 1 min. It was observed using an FEI Technai S-Twin microscope with an accelerating voltage of 200 kV.

4.8. Development of Bacterial Biofilms. *S. aureus* biofilms were developed in LB medium on 60 mm sterile polycarbonate Petri dishes. These cells (1×10^9) were spread over the Petri dish and incubated for 2 days at 37 °C.[48] Crystal violet (CV; 0.1% (w/v)) staining was used to quantify the biofilms. The CV stain was solubilized in 95% ethanol. The degree of biofilm formation was evaluated using the absorbance at 595 nm (A_{595}). The bacterial biofilms have also been cultured over implant mimic titanium foils. The morphological changes of the biofilms were determined using SEM analysis (detail in SI).

4.9. Cytotoxicity Assay. The MTT assay was used to check the biocompatibility of the ZnO-SQ nanohybrid. MG-63 cells were grown in Dulbecco's modified Eagle's medium (DMEM; HiMedia) supplemented with 10% fetal bovine serum (FBS; Gibco) and 1.0% penicillin/streptomycin

DOI: 10.1021/acsomega.8b00716
ACS Omega 2018, 3, 10877−10885

(HiMedia) and cultured at 37 °C, 5.0% CO_2, and 95% humidity.[49] These cells (1.0×10^4) were seeded in each well of a 96-well plate and cultured in 10% FBS-supplemented DMEM. The cells were incubated with various concentrations of ZnO-SQ (0−300 nM wrt SQ) for 2 h. The media have been changed with fresh media to remove excess particles, and cells were exposed to the red LED source for 30 min. After 24 h of incubation, the MTT assay was performed using an MTT assay kit (CCK003, Himedia) following the manufacture's instruction.

4.10. Hemolysis Assay. The hemolysis assay was performed on human RBCs. Ethylenediaminetetraacetate-stabilized human whole blood was centrifuged five times and redispersed in 10 mL of phosphate-buffered saline (PBS) buffer. Then, 0.1 mL of RBC solution was mixed with variable concentrations of nanohybrids. The samples were incubated at 37 °C and 100 rpm for 30 min, and then the mixture was centrifuged at 5000 rpm for 5 min. The absorption of the supernatant solution was measured at 570 nm. RBCs incubated with PBS and 1% Triton X-100 were used as negative and positive controls, respectively. All sets were prepared in triplicate. The hemolysis percentage was calculated following the reported equation.[47]

■ ASSOCIATED CONTENT

Supporting Information

The Supporting Information is available free of charge on the ACS Publications website at DOI: 10.1021/acsomega.8b00716.

Experimental details of bacteriological assays, biofilm formation, sample preparation for SEM, PI staining images, and schematic representation of band alignments (PDF)

■ AUTHOR INFORMATION

Corresponding Author

*E-mail: skpal@bose.res.in. Tel: +91 033 2335 5706-08. Fax: +91 033 2335 3477.

ORCID

Samir Kumar Pal: 0000-0001-6943-5828

Notes

The authors declare no competing financial interest.

■ ACKNOWLEDGMENTS

D.B. thanks the Department of Science and Technology (DST, India) for INSPIRE fellowship. We thank DST-SERB EMR/2016/004698, DBT-BT/PR11534/NNT/28/766/2014 DFG-RTG 1952/1, and DFG-LE967/17-1 for financial support.

■ REFERENCES

(1) Davis, S. Biomedical applications of nanotechnology—implications for drug targeting and gene therapy. *Trends Biotechnol.* **1997**, *15*, 217−224.

(2) Zhu, X.; Radovic-Moreno, A. F.; Wu, J.; Langer, R.; Shi, J. Nanomedicine in the Management of Microbial Infection - Overview and Perspectives. *Nano Today* **2014**, *9*, 478−498.

(3) Courtney, C. M.; Goodman, S. M.; McDaniel, J. A.; Madinger, N. E.; Chatterjee, A.; Nagpal, P. Photoexcited quantum dots for killing multidrug-resistant bacteria. *Nat. Mater.* **2016**, *15*, 529−534.

(4) Mekalanos, J. J. Environmental signals controlling expression of virulence determinants in bacteria. *J. Bacteriol.* **1992**, *174*, 1.

(5) Edson, J. A.; Kwon, Y. J. Design, challenge, and promise of stimuli-responsive nanoantibiotics. *Nano Convergence* **2016**, *3*, 26.

(6) Wang, S.; Huang, P.; Chen, X. Stimuli-responsive programmed specific targeting in nanomedicine. *ACS Nano* **2016**, *10*, 2991−2994.

(7) Crucho, C. I. C. The Attack of the Smart Particles: Should Bacteria Be Afraid? *ACS Med. Chem. Lett.* **2018**, *9*, 2−3.

(8) Meeker, D. G.; Jenkins, S. V.; Miller, E. K.; Beenken, K. E.; Loughran, A. J.; Powless, A.; Muldoon, T. J.; Galanzha, E. I.; Zharov, V. P.; Smeltzer, M. S.; Chen, J. Synergistic Photothermal and Antibiotic Killing of Biofilm-Associated *Staphylococcus aureus* Using Targeted Antibiotic-Loaded Gold Nanoconstructs. *ACS Infect. Dis.* **2016**, *2*, 241−250.

(9) Biju, V. Chemical modifications and bioconjugate reactions of nanomaterials for sensing, imaging, drug delivery and therapy. *Chem. Soc. Rev.* **2014**, *43*, 744−764.

(10) Hamblin, M. R.; Hasan, T. Photodynamic therapy: a new antimicrobial approach to infectious disease? *Photochem. Photobiol. Sci.* **2004**, *3*, 436−450.

(11) Boyer, J. C.; Manseau, M. P.; Murray, J. I.; van Veggel, F. C. Surface modification of upconverting NaYF4 nanoparticles with PEG-phosphate ligands for NIR (800 nm) biolabeling within the biological window. *Langmuir* **2010**, *26*, 1157−1164.

(12) Luo, S.; Zhang, E.; Su, Y.; Cheng, T.; Shi, C. A review of NIR dyes in cancer targeting and imaging. *Biomaterials* **2011**, *32*, 7127−7138.

(13) Wang, C.; Tao, H.; Cheng, L.; Liu, Z. Near-infrared light induced in vivo photodynamic therapy of cancer based on upconversion nanoparticles. *Biomaterials* **2011**, *32*, 6145−6154.

(14) Liu, K.; Liu, X.; Zeng, Q.; Zhang, Y.; Tu, L.; Liu, T.; Kong, X.; Wang, Y.; Cao, F.; Lambrechts, S. A.; et al. Covalently assembled NIR nanoplatform for simultaneous fluorescence imaging and photodynamic therapy of cancer cells. *ACS Nano* **2012**, *6*, 4054−4062.

(15) Laxminarayan, R.; Duse, A.; Wattal, C.; Zaidi, A. K. M.; Wertheim, H. F. L.; Sumpradit, N.; Vlieghe, E.; Hara, G. L.; Gould, I. M.; Goossens, H.; et al. Antibiotic resistance—the need for global solutions. *Lancet Infect. Dis.* **2013**, *13*, 1057−1098.

(16) Arias, C. A.; Murray, B. E. Antibiotic-resistant bugs in the 21st century—a clinical super-challenge. *N. Engl. J. Med.* **2009**, *360*, 439−443.

(17) U.S. Department of Health & Human Services. *Antibiotic Resistance Threats in the United States, 2013*; CDC: Atlanta, 2013.

(18) Huh, A. J.; Kwon, Y. J. "Nanoantibiotics": a new paradigm for treating infectious diseases using nanomaterials in the antibiotics resistant era. *J. Controlled Release* **2011**, *156*, 128−145.

(19) Mansour, H. M.; Rhee, Y.-S.; Wu, X. Nanomedicine in pulmonary delivery. *Int. J. Nanomed.* **2009**, *4*, 299.

(20) Karim, M. N.; Singh, M.; Weerathunge, P.; Bian, P.; Zheng, R.; Dekiwadia, C.; Ahmed, T.; Walia, S.; Della Gaspera, E.; Singh, S.; Ramanathan, R.; Bansal, V. Visible-Light-Triggered Reactive-Oxygen-Species-Mediated Antibacterial Activity of Peroxidase-Mimic CuO Nanorods. *ACS Appl. Nano Mater.* **2018**, 1694−1704.

(21) Percival, S. L.; Suleman, L.; Vuotto, C.; Donelli, G. Healthcare-associated infections, medical devices and biofilms: risk, tolerance and control. *J. Med. Microbiol.* **2015**, *64*, 323−334.

(22) Flemming, H.-C.; Wingender, J. The biofilm matrix. *Nat. Rev. Microbiol.* **2010**, *8*, 623−633.

(23) Wang, L.-S.; Gupta, A.; Rotello, V. M. Nanomaterials for the treatment of bacterial biofilms. *ACS Infect. Dis.* **2016**, *2*, 3−4.

(24) Fux, C. A.; Costerton, J. W.; Stewart, P. S.; Stoodley, P. Survival strategies of infectious biofilms. *Trends Microbiol.* **2005**, *13*, 34−40.

(25) Geilich, B. M.; Gelfat, I.; Sridhar, S.; van de Ven, A. L.; Webster, T. J. Superparamagnetic iron oxide-encapsulating polymersome nanocarriers for biofilm eradication. *Biomaterials* **2017**, *119*, 78−85.

(26) Dennison, D. K.; Huerzeler, M. B.; Quinones, C.; Caffesse, R. G. Contaminated implant surfaces: an in vitro comparison of implant surface coating and treatment modalities for decontamination. *J. Periodontol.* **1994**, *65*, 942−948.

(27) Hunter, R. C.; Beveridge, T. J. Application of a pH-sensitive fluoroprobe (C-SNARF-4) for pH microenvironment analysis in

DOI: 10.1021/acsomega.8b00716
ACS Omega 2018, 3, 10877−10885

Pseudomonas aeruginosa biofilms. *Appl. Environ. Microbiol.* **2005**, *71*, 2501−2510.
(28) Zhang, Z. Y.; Xu, Y. D.; Ma, Y. Y.; Qiu, L. L.; Wang, Y.; Kong, J. L.; Xiong, H. M. Biodegradable ZnO@ polymer Core-Shell Nanocarriers: pH-Triggered Release of Doxorubicin In Vitro. *Angew. Chem., Int. Ed.* **2013**, *52*, 4127−4131.
(29) Raghupathi, K. R.; Koodali, R. T.; Manna, A. C. Size-dependent bacterial growth inhibition and mechanism of antibacterial activity of zinc oxide nanoparticles. *Langmuir* **2011**, *27*, 4020−4028.
(30) Chaudhuri, S.; Sardar, S.; Bagchi, D.; Dutta, S.; Debnath, S.; Saha, P.; Lemmens, P.; Pal, S. K. Photoinduced dynamics and toxicity of a cancer drug in proximity of inorganic nanoparticles under visible light. *ChemPhysChem* **2016**, *17*, 270−277.
(31) Sardar, S.; Chaudhuri, S.; Kar, P.; Sarkar, S.; Lemmens, P.; Pal, S. K. Direct observation of key photoinduced dynamics in a potential nano-delivery vehicle of cancer drugs. *Phys. Chem. Chem. Phys.* **2015**, *17*, 166−177.
(32) Page, K.; Wilson, M.; Parkin, I. P. Antimicrobial surfaces and their potential in reducing the role of the inanimate environment in the incidence of hospital-acquired infections. *J. Mater. Chem.* **2009**, *19*, 3819−3831.
(33) Park, J.; Barolo, C.; Sauvage, F.; Barbero, N.; Benzi, C.; Quagliotto, P.; Coluccia, S.; Di Censo, D.; Gratzel, M.; Nazeeruddin, M. K.; Viscardi, G. Symmetric vs. asymmetric squaraines as photosensitisers in mesoscopic injection solar cells: a structure-property relationship study. *Chem. Commun.* **2012**, *48*, 2782−2784.
(34) Patwari, J.; Sardar, S.; Liu, B.; Lemmens, P.; Pal, S. K. Three-in-one approach towards efficient organic dye-sensitized solar cells: aggregation suppression, panchromatic absorption and resonance energy transfer. *Beilstein J. Nanotechnol.* **2017**, *8*, 1705−1713.
(35) Kuchlyan, J.; Kundu, N.; Banik, D.; Roy, A.; Sarkar, N. Spectroscopy and Fluorescence Lifetime Imaging Microscopy To Probe the Interaction of Bovine Serum Albumin with Graphene Oxide. *Langmuir* **2015**, *31*, 13793−13801.
(36) Anderson, N. A.; Lian, T. Ultrafast electron transfer at the molecule-semiconductor nanoparticle interface. *Annu. Rev. Phys. Chem.* **2005**, *56*, 491−519.
(37) Bagchi, D.; Chaudhuri, S.; Sardar, S.; Choudhury, S.; Polley, N.; Lemmens, P.; Pal, S. K. Modulation of stability and functionality of a phyto-antioxidant by weakly interacting metal ions: curcumin in aqueous solution. *RSC Adv.* **2015**, *5*, 102516−102524.
(38) Flors, C.; Fryer, M. J.; Waring, J.; Reeder, B.; Bechtold, U.; Mullineaux, P. M.; Nonell, S.; Wilson, M. T.; Baker, N. R. Imaging the production of singlet oxygen in vivo using a new fluorescent sensor, Singlet Oxygen Sensor Green. *J. Exp. Bot.* **2006**, *57*, 1725−1734.
(39) Li, X.; Robinson, S. M.; Gupta, A.; Saha, K.; Jiang, Z.; Moyano, D. F.; Sahar, A.; Riley, M. A.; Rotello, V. M. Functional gold nanoparticles as potent antimicrobial agents against multi-drug-resistant bacteria. *ACS Nano* **2014**, *8*, 10682−10686.
(40) Huang, Z.; Zheng, X.; Yan, D.; Yin, G.; Liao, X.; Kang, Y.; Yao, Y.; Huang, D.; Hao, B. Toxicological effect of ZnO nanoparticles based on bacteria. *Langmuir* **2008**, *24*, 4140−4144.
(41) Wahab, R.; Kaushik, N. K.; Kaushik, N.; Choi, E. H.; Umar, A.; Dwivedi, S.; Musarrat, J.; Al-Khedhairy, A. A. ZnO nanoparticles induces cell death in malignant human T98G gliomas, KB and non-malignant HEK cells. *J. Biomed. Nanotechnol.* **2013**, *9*, 1181−1189.
(42) Bagchi, D.; Maji, T. K.; Sardar, S.; Lemmens, P.; Bhattacharya, C.; Karmakar, D.; Pal, S. K. Sensitized ZnO nanorod assemblies to detect heavy metal contaminated phytomedicines: spectroscopic and simulation studies. *Phys. Chem. Chem. Phys.* **2017**, *19*, 2503−2513.
(43) Chaudhuri, S.; Sardar, S.; Bagchi, D.; Singha, S. S.; Lemmens, P.; Pal, S. K. Sensitization of an endogenous photosensitizer: electronic spectroscopy of riboflavin in the proximity of semiconductor, insulator, and metal nanoparticles. *J. Phys. Chem. A* **2015**, *119*, 4162−4169.
(44) Seddigi, Z. S.; Ahmed, S. A.; Sardar, S.; Pal, S. K. Ultrafast dynamics at the zinc phthalocyanine/zinc oxide nanohybrid interface for efficient solar light harvesting in the near red region. *Sol. Energy Mater. Sol. Cells* **2015**, *143*, 63−71.
(45) Mor, A.; Koh, E.; Weiner, L.; Rosenwasser, S.; Sibony-Benyamini, H.; Fluhr, R. Singlet oxygen signatures are detected independent of light or chloroplasts in response to multiple stresses. *Plant Physiol.* **2014**, *165*, 249−261.
(46) Zheng, K.; Setyawati, M. I.; Leong, D. T.; Xie, J. Antimicrobial Gold Nanoclusters. *ACS Nano* **2017**, *11*, 6904−6910.
(47) Huo, S.; Jiang, Y.; Gupta, A.; Jiang, Z.; Landis, R. F.; Hou, S.; Liang, X.-J.; Rotello, V. M. Fully zwitterionic nanoparticle antimicrobial agents through tuning of core size and ligand structure. *ACS Nano* **2016**, *10*, 8732−8737.
(48) Bagchi, D.; Dutta, S.; Singh, P.; Chaudhuri, S.; Pal, S. K. Essential Dynamics of an Effective Phototherapeutic Drug in a Nanoscopic Delivery Vehicle: Psoralen in Ethosomes for Biofilm Treatment. *ACS Omega* **2017**, *2*, 1850−1857.
(49) Singh, P.; Choudhury, S.; Kulanthaivel, S.; Bagchi, D.; Banerjee, I.; Ahmed, S. A.; Pal, S. K. Photo-triggered destabilization of nanoscopic vehicles by dihydroindolizine for enhanced anticancer drug delivery in cervical carcinoma. *Colloids Surf., B* **2018**, *162*, 202−211.

DOI: 10.1021/acsomega.8b00716
ACS Omega 2018, 3, 10877−10885